AGU PUBLICATIONS

JGR

Journal of Geophysical Research: Atmospheres

RESEARCH ARTICLE
10.1002/2014JD021562

Key Points:
- Polar tides
- Seasonal variation
- Nonlinear interaction

Supporting Information:
- Readme
- Text S1
- Figure S1a
- Figure S1b
- Figure S2a
- Figure S2b
- Figure S3
- Figure S4
- Figure S5

Correspondence to:
J. Du,
jian.du@louisville.edu

Citation:
Du, J., W. E. Ward, and F. C. Cooper (2014), The character of polar tidal signatures in the extended Canadian Middle Atmosphere Model, *J. Geophys. Res. Atmos.*, *119*, 5928–5948, doi:10.1002/2014JD021562.

Received 29 JAN 2014
Accepted 5 MAY 2014
Accepted article online 9 MAY 2014
Published online 28 MAY 2014

The character of polar tidal signatures in the extended Canadian Middle Atmosphere Model

J. Du[1], W. E. Ward[2], and F. C. Cooper[3]

[1]Department of Physics and Astronomy, University of Louisville, Louisville, Kentucky, USA, [2]Department of Physics, University of New Brunswick, Fredericton, New Brunswick, Canada, [3]Department of Mathematics, University College London, London, UK

Abstract The characteristics of the diurnal, semidiurnal, and terdiurnal tides (zonal wave numbers −5 to +5 in temperature and zonal wind) in the polar mesosphere and lower thermosphere region as simulated by the extended Canadian Middle Atmosphere Model are examined. The most significant diurnal, semidiurnal, and terdiurnal tides in the polar regions are Ds0, Dw1, and De1; Sw3, Sw2, Sw1, Ss0, Se1, and Se2; and Tw3, Ts0, and Tw1, respectively, and their latitudinal structures, seasonal variations, and hemispheric asymmetries noted. Of these components, Ds0, Tw1, Ts0, and Tw3 exhibit a seasonally symmetric variation with both hemispheres strengthening simultaneously. On the other hand, Dw1 strengthens asymmetrically so that when one hemisphere is strong, the other is weak. The remainder show no seasonal tendency but vacillate on shorter than seasonal time scales in a symmetric or antisymmetric manner at different times of the year. Global-scale correlations of the amplitudes of the migrating tides Dw1/Sw2 and the stationary planetary wave 1 and the assumed "child" nonmigrating tides are also examined. The results indicate that the correlations are highly time scale-dependent and the significant correlations seen with the original time series are mainly due to longer-term variations (>18 days). There are no consistent global correlations associated with the short-term variations (<18 days) among these waves.

1. Introduction

The polar regions (>60°N/S) in the mesosphere and lower thermosphere (MLT) are the site of unique and rich tidal features. In combination, they are the primary driver of the large-scale dynamical structure and the variability in this region. Although aspects of individual tidal components have been observed and discussed, there are no papers that discuss the role and impact of these components as a whole. This paper takes on this task using output from a realistic general circulation model (GCM). The intent is to provide the general perspective from the model in order to encourage observational progress in their validation and to further work on the examination of the role of these tides in the MLT and above. Earlier theoretical and observational studies have shown that the tidal wind field in the vicinity of the geographical poles possesses a zonal wave number 1 structure, while the structure of scalar variables (such as temperature, density, and pressure) has a zonal wave number 0 character [*Hernandez et al.,* 1992a, 1992b; *Portnyagin et al.*, 1998; *Forbes et al.*, 1999]. Other than these zonal wave number 0 and 1 tides, many other tidal components contribute to the tidal fields in this region. Some maximize within the polar regions and others maximize at low and/or middle latitudes but still have significant amplitudes in the polar regions [*Du et al.*, 2007; *Du and Ward*, 2010].

There have been extensive polar tidal studies of the neutral MLT region from the ground-based observations in the Southern Hemisphere (SH) high latitudes centered around the South Pole, based on optical observations of the winds and OH-emission rates [*Hernandez et al.*, 1993, 1995; *Fraser et al.,* 1995], and radar observations [*Forbes et al.*, 1995; *Portnyagin et al.*, 1997, 1998; *Baumgaertner et al.*, 2005, 2006; *Murphy et al.*, 2006]. Ground-based wind measurements have also been made at various locations in the Arctic [*Oznovich et al.*, 1997; *Hocking*, 2001; *Fisher et al.*, 2002; *Kishore et al.*, 2002; *Mitchell et al.*, 2002; *Aso*, 2003; *Wu et al.*, 2003; *Portnyagin et al.*, 2004; *Merzlyakov et al.*, 2005; *Nozawa et al.*, 2005; *Singer et al.*, 2005; *Hoffmann et al.*, 2007; *Manson et al.*, 2006, 2009]. Several satellite data sets [*Angelats i Coll and Forbes*, 2002; *Manson et al.*, 2004; *Forbes and Wu*, 2006; *Iimura et al.*, 2009, 2010] and a few models [*Miyahara et al.*, 1999; *Yamashita et al.*, 2002; *Angelats i Coll and Forbes*, 2002; *Mayr et al.*, 2005; *Aso*, 2007; *Du and Ward*, 2010] have also been employed to study the structure of specific tidal components in the high-latitude MLT region.

In previous studies, the nonmigrating Sw1 tidal component has received the most attention. (Throughout the remainder of this paper, we utilize the notation Dws or Des to denote a westward or eastward propagating diurnal tide, respectively, with zonal wave number *s*. The standing oscillations are denoted as Ds0. Of these tidal components, Dw1 is the migrating tides and the rest are nonmigrating tides.). In the SH, the associated wind field was found to dominate poleward of 75°S with a distinctive seasonal variation with maxima during nonwinter months [*Forbes et al.,* 1995, 1999; *Portnyagin et al.*, 1998; *Lau et al.*, 2006]. The mechanism responsible for the existence of this oscillation has also been extensively studied using correlations between various diagnosed components in observed time series [*Forbes et al.*, 1995; *Baumgaertner et al.*, 2005, 2006; *Murphy et al.*, 2006; *Smith et al.*, 2007; *Xu et al.*, 2009] and model analyses [*Hagan and Roble*, 2001; *Angelats i Coll and Forbes*, 2002; *Yamashita et al.*, 2002; *Aso*, 2007; *Chang et al.,* 2009; *Liu et al.,* 2010]. Most of the above studies attribute the source of Sw1 to nonlinear interactions between the migrating semidiurnal tide Sw2 and the stationary planetary wave 1 (SPW1), although a couple of authors note the potential of zonally asymmetric thermal forcing in the troposphere as another mechanism [*Forbes et al.*, 1999; *Hagan and Forbes*, 2003].

Recent analyses from radar measurements at multiple stations on the coast of Antarctica by *Murphy et al.* [2006] determined that the semidiurnal tidal wind field is a mixture of Sw1, Sw2, Sw3, and Ss0. *Portnyagin et al.* [2004] concluded that the migrating tides are dominant for both diurnal and semidiurnal oscillations in the southern Arctic (65–70°N) during all months, but with some indications of nonmigrating tides in May–June. *Manson et al.* [2009], based on analysis of the Svalbard and Eureka tides during 2006/2007, showed that at latitudes near 80°N, the semidiurnal migrating tide Sw2 is dominant in summer, while the nonmigrating Sw1 and Sw3 occur most often during equinoctial or early summer months. *Forbes and Wu* [2006] discussed the global tidal field (80°S–80°N), using temperatures from Microwave Limb Sounder (MLS)/Upper Atmosphere Research Satellite (UARS) (1991–1997) at heights of 25–86 km. Their study confirmed the presence of Sw1 and Sw3 in the polar regions. Using TIMED Doppler Interferometer (TIDI)/Thermosphere Ionosphere Mesosphere Energetics and Dynamics (TIMED) satellite wind measurements, *Iimura et al.* [2009] presented evidence for the existence of Sw1 in the Antarctic MLT meridional wind field prior to the austral summer solstice. This wave achieves peak amplitude near 20 m/s at 90 km and extends latitudinally from the pole to 60°S. Significant though weaker Ss0 and Sw3 amplitudes were also found. In a companion paper, using the same data set, *Iimura et al.* [2010] found the existence of the same nonmigrating semidiurnal tides over the Arctic, although Sw1 exhibited different features between the poles. These differences are thought to result from differences in excitation mechanisms and their efficiency and/or in variations in the propagation conditions between the Arctic and Antarctic.

In contrast to the semidiurnal tides, reports on diurnal and terdiurnal tidal components in the polar regions are relatively rare. The migrating diurnal tide Dw1 seems to be a dominant feature in the ground-based wind observations in the Antarctic all year round [*Portnyagin et al.*, 1998; *Murphy et al.*, 2006; *Lübken et al.,* 2011]. For the Arctic, *Manson et al.* [2009] found that the nonmigrating Ds0 and Dw2 components dominate the migrating diurnal tide Dw1 during the nonsummer months. Using MLS/UARS temperature data, *Forbes and Wu* [2006] confirmed the presence of Dw1, Ds0, and Dw2 and proposed that the latter might be generated by nonlinear interactions between Dw1 and SPW1.

There are only a handful of reports on the terdiurnal tides in the polar regions from ground-based observations in the Arctic [*Oznovich et al.*, 1997; *Younger et al.*, 2002], satellite observation [*Forbes and Wu*, 2006], and modeling studies which mainly focus on the migrating terdiurnal tide Tw3 [*Akmaev*, 2001; *Smith and Ortland*, 2001]. A recent study by *Du and Ward* [2010] presented the morphology of the terdiurnal tides (including the migrating and 10 nonmigrating components) in the MLT region as diagnosed from the extended Canadian Middle Atmospheric Model (eCMAM). The migrating terdiurnal tide Tw3 maximizes at middle/high latitudes with significant amplitudes in the upper MLT region and distinctive seasonal variations at different height ranges. The nonmigrating terdiurnal components Te2, Te1, Ts0, Tw1, and Tw2 maximize in the polar regions (centered on ~65°–75°) in both hemispheres with amplitudes between 2 and 10 m/s for the zonal wind.

In this paper, we use the third year of a 4 year run of the eCMAM to summarize the significant migrating and nonmigrating diurnal, semidiurnal, and terdiurnal tides in the polar regions. The eCMAM is a three-dimensional GCM with a well-resolved troposphere and an upper boundary at 2×10^{-7} mbar (~210 km)

[*Beagley et al.*, 2000; *Fomichev et al.*, 2002]. Previous studies have shown that this eCMAM run is in good qualitative agreement with Wind Imaging Interferometer (WINDII) and High Resolution Doppler Interferometer (HRDI)/UARS observations of the mean winds and the Dw1 [*Beagley et al.*, 2000; *Fomichev et al.*, 2002; *McLandress*, 2002]. The model includes realistic tidal forcing due to radiative heating, convective processes, and latent heat release (see *Scinocca and McFarlane* [2004] for details) and uses the gravity wave breaking parameterization of *Hines* [1997a, 1997b]. These processes have been shown to provide the forcing necessary to generate the migrating and nonmigrating tides [*McLandress*, 1998, 2002; *Ward et al.*, 2005; *Du et al.*, 2007; *Du and Ward*, 2010].

This particular model run has also been extensively validated against recent tidal observations from ground-based and satellite instruments and other model simulations [*Du et al.*, 2007; *Zeng et al.*, 2008; *Du*, 2008; *Ward et al.*, 2010; *Du and Ward*, 2010; *Chang et al.*, 2012; *Davis et al.*, 2013]. It has been shown that eCMAM can resolve latitudinal structures and seasonal variations that are consistent with observations for most tidal components. Exact duplication of observed tidal features is not achieved with this model run (to date, no free running GCM achieves this) but the similarities are sufficient for the purposes of this paper. The tidal variability and relationships among waves are self-consistently generated within the model so that the global aspects of the tidal fields can be explored and a basis for comparisons with observations provided.

The analysis of the tidal fields proceeds as follows. Spatial spectral analysis (as described by *Ward et al.* [2005], *Du et al.* [2007], and *Du and Ward* [2010]) is applied to the modelled temperature and horizontal wind fields to obtain the amplitudes and phases of the diurnal, semidiurnal, and terdiurnal tides for zonal wave numbers -5 to +5. The significant tidal components in the polar regions generated by the model are then identified and their seasonal variability examined. Correlations between waves (which have been used as a sign of nonlinear interaction in previous works) are calculated to examine the extent to which these proposed interactions are present in the model in a global sense.

This study has several objectives.

1. One objective is to broaden the general appreciation for the complexity of the tides in the polar regions. We provide an overview of the polar tides (diurnal, semidiurnal, and terdiurnal tides from zonal wave number $s = -5$ to +5) based on our model results and substantiated through comparisons with published studies. To our knowledge, there have not been any reviews of polar tides over the past three decades with the extent and detail provided here. The model results reveal some tidal characteristics that have not previously been reported. We also identify tidal signatures in the lower thermosphere (to a height of 135 km), since these components will influence geomagnetic conditions and be of interest to the ionospheric community. We hope that our presentation of the character of the polar tides will stimulate more complete observations and further modeling studies.
2. The second objective is to identify topics that need to be further studied in order to better understand the tidal seasonal variability. Latitudinal symmetries and asymmetries are observed with different components and the cause of these variations remains to be determined.
3. The third objective is to refine the manner in which correlation analysis is used as an indicator of nonlinear interactions. Correlations between the amplitudes of two proposed pairs of waves (Dw1 + SPW1 produce Ds0 + Dw2; Sw2 + SPW1 produce Sw1 + Sw3) are examined. Strong correlations are found with the full time series. However, after applying a high-pass filter to the time series, the correlations over short time scales are not found to be significant. More discussion on the interpretation of time scale-dependent correlations as indicators of nonlinear interactions is needed.

Given these objectives (the purpose of this paper is not the generation of a climatology of polar tidal signatures), 1 year of data from the model is a suitable platform for revealing the features and dynamical properties of the tides necessary for the above purposes.

The paper is organized as follows. We begin by briefly describing the eCMAM and our data analysis procedures in section 2. In section 3, we first identify significant polar tidal components in the winds and temperature fields and then present their annual mean latitudinal structures. The seasonal variations of the significant tides in the polar regions are provided in section 4. Section 5 presents the global correlation analysis of the total time series and the time series after the high-/low-pass filter between the assumed parent waves Dw1/SPW1 and their child waves Dw2/Ds0, and the assumed parent waves Sw2/SPW1 and their assumed child waves Sw1/Sw3. The conclusions of this study are provided in section 6.

2. Description of the eCMAM and Data Analysis Method

The eCMAM and the particular model run used for the present study have been extensively described by the model developers [*Beagley et al.,* 2000; *Fomichev et al.,* 2002] and in previous studies [*McLandress*, 2002; *Ward et al.*, 2005; *Du et al.*, 2007; *Du and Ward*, 2010]. Here we only give a brief description of the model and data analysis method.

The eCMAM is a global, three-dimensional spectral GCM extending from the Earth's surface to about 210 km. It has 70 vertical layers and the latitudinal-longitudinal resolution is ~6°×6° near the equator. The vertical resolution in the MLT region is ~ 3 km. Physical parameterizations appropriate to the MLT region (e.g., EUV, SR-band radiation, CO_2 nonlocal thermal equilibrium (LTE) effects, parameterized chemical heating, molecular viscosity, molecular thermal diffusion, ion drag, and modified gravity wave parameterization) have been implemented. Tidal oscillations are generated self-consistently through internal processes associated with absorption of short- and long-wave radiation, large-scale condensation, and convective heating.

Output from the third year of a 4 year run is used for this study. The model sampling time interval for the run is 3 h and the model output is expressed as frequency/zonal wave number (σ/s) fields. By summing over the spatial part of the spherical harmonics, complex amplitudes as a function of frequency are obtained at each latitude and height for each time step. Fourier transformation of windowed time series of these amplitudes is used to generate the tidal components presented in this paper. For the present study, temperature and horizontal winds from the model run are analyzed to delineate the character of diurnal, semidiurnal, and terdiurnal tides for $s = -5$ to +5.

Although the terdiurnal tidal period is close to the Nyquist period of our sampling (3 h), the tidal estimates presented in this paper are representative of the actual tidal components. The spectral power in the model decreases rapidly for higher frequencies so aliasing is minor. This was verified using spectral analyses of a run with half-hour sampling. The spectra obtained using the half-hour sampling are marginally different from the spectra obtained using a degraded sampling of 3 h for the same run (details of this comparison are provided in *Du and Ward* [2010]). Furthermore, the model effectively samples the wind and temperature fields from 60 longitudes (equivalent of 60 ground-based stations) at each latitude circle and each longitude (station) is sampled eight times a day. The 3 h sampling frequency from the model is sufficient to study the terdiurnal tide.

3. Significant Polar Tides and Their Latitudinal Structures

The latitudinal form of the significant tidal components determines the meridional structure of the net tidal field. To characterize this structure, the significant diurnal, semidiurnal, and terdiurnal components in polar regions are identified using annual means of the horizontal wind and temperature. Included are components which maximize in the polar regions and those which maximize elsewhere but have significant polar extent. Previous studies have shown that eCMAM simulations generate latitudinal structures of the tides which compare well with observations and other models [*Du et al.,* 2007; *Du,* 2008; *Chang et al.,* 2012]. The annual mean latitudinal structure is calculated with monthly mean amplitude information only, phase is not considered since it varies with time. Averaging amplitude over time with phase information included can cause amplitude cancelation and is not suitable for our purposes here. The figures in this section will be focused on zonal wind, similar figures for meridional wind and temperature are provided as supporting information (note that the significant components are different depending on the parameter being considered).

3.1. Significant Polar Tidal Components

For this paper, 11 components for each tidal period were analyzed (from $s = -5$ to +5). The wave numbers identify tidal "components" or "tides"; and positive (negative) zonal wave numbers imply westward (eastward) propagation. Figure 1 shows the relative significance of the various diurnal, semidiurnal and terdiurnal components and their variability with height in the polar regions for zonal wind (U). The annual "maximum" amplitudes (m/s) of the tidal components over the Southern Polar Region (SPR: 60°S–90°S; Figure 1) and the Northern Polar Region (NPR: 60°N–90°N; Figure 1) are presented as a function of zonal wave number and height (from 60 to 120 km). The annual maximum amplitudes for a tidal component are sought over its 12 monthly mean amplitudes in the SPR and NRP, respectively. The top row of Figure 1 is for the diurnal tide and the middle and bottom rows are for semidiurnal and terdiurnal tides, respectively.

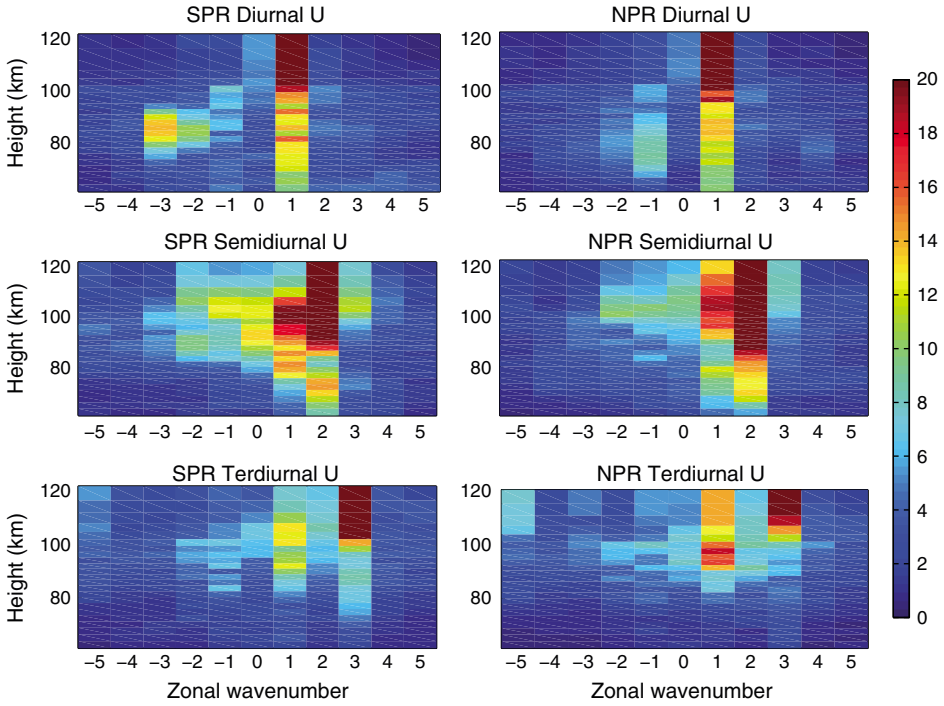

Figure 1. Annual "maximum" zonal wind (*U*) tidal amplitudes (m/s) as a function of zonal wave number (from −5 to +5) and height (from 60 to 120 km) in the Southern Polar Region (SPR) and the Northern Polar Region (NPR). Positive wave numbers are for the westward propagating components, and negative wave numbers are eastward. (top row) Diurnal, (middle row) semidiurnal, and (bottom row) terdiurnal tides.

The color scale for both polar regions is the same, so that the maximum amplitude for the same tidal component can be directly compared.

The most significant diurnal component for zonal wind (Figure 1, top row) is Dw1 (10–15 m/s). Other significant components include De1 (below 100 km), Ds0 (above 100 km) in both polar regions, and De3 and De2 (70–90 km) in the SPR. Meridional wind (Figure S1b in the supporting information) shows similar components as the zonal wind. For the diurnal temperature field in both polar regions (Figure S1a), Ds0 is the most significant component. Considering both the temperature and wind fields, the most significant diurnal tidal components in both polar regions are Ds0, Dw1, and De1. One interesting feature is the stronger presence of De3 (70–90 km) in the SPR and its relative absence in the NPR.

For the zonal wind semidiurnal tides in the polar regions (Figure 1, middle row), the most significant components are Sw2 and Sw1 (both ~15 m/s). Ss0 and Se1 are slightly weaker, with their amplitudes being greater in the SPR (12 m/s) than the NPR (8 m/s). Above 100 km, Sw3 and Se2 have significant amplitudes (>8 m/s). The same components are dominant in the temperature field (Figure S1a) but with different relative amplitudes than in the wind fields. The Ss0 maximum amplitude is stronger than Sw1 and the maximum amplitude of Se2 is comparable to that of Sw2, Ss0, and Se1. Overall, the most significant semidiurnal tidal components in the polar regions are Sw3, Sw2, Sw1, Ss0, Se1, and Se2.

The polar terdiurnal tidal components in the zonal wind are presented in Figure 1 (bottom row). The dominant components are Tw3 (>15 m/s) and Tw1 (15 m/s in the NPR and slightly weaker in the SPR). The amplitude of Tw2, Ts0, Te1, Te2, and Te5 is also significant, with stronger maximum amplitude in the NPR (8–10 m/s) than the SPR (5–7 m/s). Ts0 and Tw3 are the most significant components for the temperature field (Figure S1a). Overall, we consider Tw3, Ts0, and Tw1 as the most significant terdiurnal components in the polar regions.

3.2. Latitudinal Structure of the Significant Polar Tides

The latitudinal structure of the significant diurnal and semidiurnal components in the polar regions is presented in Figure 2. Included are the annual mean amplitudes of the diurnal tidal components De1, Ds0, and Dw1 (Figure 2, top row) and the semidiurnal tidal components Sw1, Sw2, Sw3 (Figure 2, middle row), and Se1,

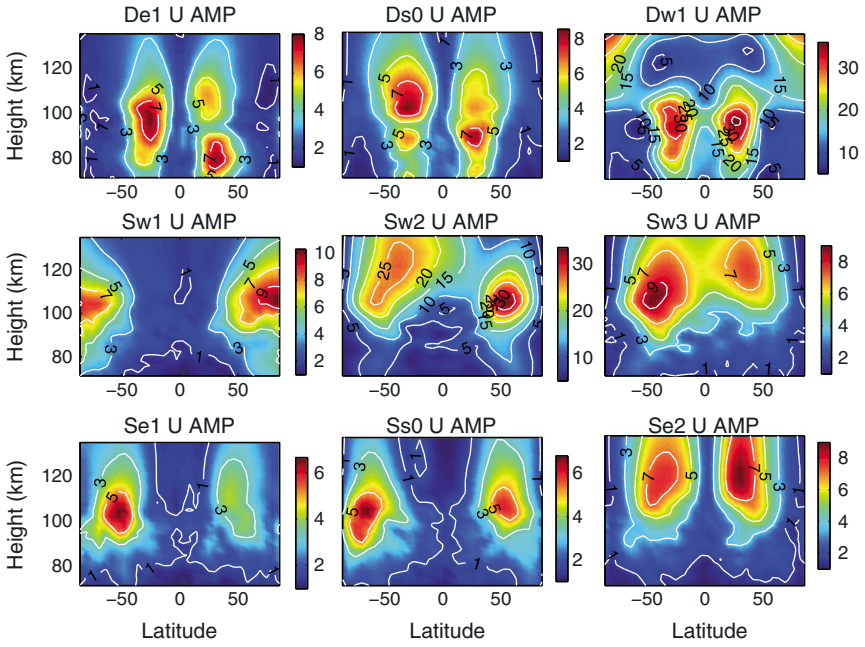

Figure 2. Annual mean latitudinal structures of the zonal wind (*U*) amplitude (m/s) for the (top row) diurnal tidal components De1, Ds0, and Dw1, the (middle row) semidiurnal tidal components Sw1, Sw2, and Sw3, and the (bottom row) semidiurnal tidal components Se1, Ss0, and Se2 from eCMAM. The height range is from 75 to 130 km and the latitude range is from −85.7° to 85.7° (SH latitude is negative and NH latitude is positive).

Ss0, Se2 (Figure 2, bottom row) as a function of latitude and altitude for zonal wind (*U*). The latitudinal structure for the meridional wind and temperature fields for these components is provided as Figures S2a and S2b in the supporting information. The annual mean amplitudes of the terdiurnal tidal components Tw3, Ts0, and Tw1 have been presented in *Du and Ward* [2010]. The altitude range is limited to 70–135 km and the latitude range is from −85.7° to 85.7° (SH latitude is negative and NH latitude is positive). Note that the amplitude color scales in Figure 2 (and Figure S2) are different for the various zonal wave number components. The salient features of these structures are discussed below.

For the De1 *U* field (Figure 2, top row), two maxima (7–8 m/s) are symmetrically located in the low and middle latitudes (10°–50°) of each hemisphere, centered on 30°–40°. The maximum in the SH is located between 90 and 105 km while the feature in the NH splits into two maxima with a minimum amplitude at ~ 90 km. An interesting feature is the difference in latitude structure above and below 90 km in all three fields (this is more obvious in the meridional wind and temperature fields provided in Figure S2) which suggests that different Hough modes are associated with this tidal component in these two regions. There are secondary maxima around the poles with much weaker amplitude (3–4 m/s) for the winds.

The overall latitude structure of the Ds0 fields is similar to that of the De1 fields but with broader features which extend into the polar regions. A change in structure at 100 km also occurs with this component (more obvious in the *V* and *T* fields; see Figure S2). The Ds0 component is more asymmetric than De1. The *U* maximum (7–9 m/s) in the SH is located between 30° and 40°S, and 95 and 110 km, whereas the maximum (7 m/s) in the NH is located in a smaller latitude band and around 90 km. The hemispheric asymmetry is also present for the *T* and *V* fields (Figure S2).

Below 100 km, the migrating Dw1 component conforms to the now well-known structure [*Hagan and Forbes,* 2001; *Zhang et al.,* 2006]. Here there are two maxima (>30 m/s for *U* and >50 m/s for *V*) symmetrically located between 10°–50° in each hemisphere and centered at 30° (20°) for *U* (*V*). Again, there is a change in structure above 100 km: Dw1 has two maxima (>20 m/s for both winds) symmetrically located over the polar regions of each hemisphere with amplitude increasing with height. These are likely excited locally by the EUV absorption. The *T* field (Figure S2a) maximizes (amplitude > 20 K) in the equatorial region, between 100 and 110 km and has two secondary maxima (>5 K) in the subtropics at

similar altitudes. This structure extends to about 120 km. Above 120 km, there are two broad features symmetrically locating between 10°N(S) and the poles of both hemispheres with maxima (>25 K) centered at 30–40°N/S. The amplitudes associated with the features above 120 km increase with height.

For the Sw1 *U* field (Figure 2, middle row), the maximum annual mean amplitudes (8–10 m/s) are located in the polar region of each hemisphere between 100 and 110 km. The amplitude in the NH is slightly stronger than that in the SH. Besides the polar maxima, there are weaker secondary maxima (3–5 m/s) in the subtropics for the *V* field (Figure S2b). The temperature field (Figure S2a) has a different latitudinal structure than the winds with broad features extending between the poles with three peaks greater than 3 K (one at the equator and two in the midlatitudes of each hemisphere).

For the migrating semidiurnal Sw2 *U* field, a region of significant amplitude extends from pole to pole with maxima in both hemispheres in the middle to high latitudes. The maximum amplitude (>25 m/s) in the SH is located at 50° at 105 km. Above 110 km, the feature becomes broader than below and is centered at 40°S. The NH maximum is much more compact, stronger, and at lower altitudes than its SH counterpart. The maximum (>30 m/s) is located between 50° and 55°N, and 95 and 110 km. The *V* field (Figure S2b) has a similar latitudinal structure as the *U* field except that the *V* field has an extra subtropical maximum in the NH. The Sw2 *T* latitudinal structure (Figure S2a) is quite different from the winds with a broad feature ranging from 60°N and 60°S with significant hemispheric asymmetry (the maximum of > 25 K is located between 5°N and 20°S, and 110 and 130 km).

The latitudinal structure of the Sw3 *U* field has two maxima located in the middle and high latitudes of each hemisphere. The SH maximum (>9 m/s) is located between 10° and 60°S and centered at 45°S and 100–110 km. The NH maximum is located slightly higher (centered at 40°–45°N and 120 km) and weaker (7 m/s) than the SH counterpart. The Sw3 *V* field (Figure S2b) is very similar to the *U* field in terms of both its latitudinal structure and amplitude. There is a broad region of enhanced amplitude in the *T* field (Figure S2a) extending from 70°N to 70°S with the maximum amplitude (7–9 K) located in the equatorial region and centered at 10°N above 110 km.

The Se1 *U* field (Figure 2, bottom row) maximizes in the middle/high latitudes (30°–70°) of each hemisphere with the SH maximum (>5 m/s) being stronger than the NH one (3 m/s). The maxima are centered at 50°N/S and between 90 and 110 km, with the NH maximum located slightly higher than the SH maximum. The *V* field latitudinal structure and characteristics (Figure S2b) are very similar to those of the *U* field, but with the maxima located slightly closer to the equator at 40°N/S. The amplitude of the *T* field (Figure S2a) is significant from pole to pole and includes three peaks. One peak (3–4 K) is located in the SPR centered on 60°S, the second peak (3 K) is located in the NH middle and high latitudes centered on 50°N, and the third (2–3 K) is located in the equatorial region.

The Ss0 *U* field maximizes in the polar regions (5–8 m/s). The SH maximum is centered at 70°S and between 100 and 110 km. The NH maximum is centered at the same height but at a slightly equatorward latitude (60°N). The *V* field (Figure S2b) is very similar to the *U* field but with stronger annual mean amplitude (7 m/s as opposed to 5 m/s for *U*) and the NH maximum is located at 50°N. The *T* field (Figure S2a) is characterized by a broad structure from pole to pole with maxima in amplitude (5–6 K) located in the polar regions and secondary maxima (2–3 K) in the midlatitudes of each hemisphere.

The Se2 *U* field has two maxima located symmetrically in the middle and high latitudes of each hemisphere and centered at 30°–40°N/S. The NH maximum (7–9 m/s) tends to be slightly stronger than the SH maximum (7 m/s). The *T* field (Figure S2a) has a similar latitudinal structure as the *U* field and the hemispheric asymmetry is more obvious than in the *U* field. The Se2 *V* field (Figure S2b) is very different from the *U* and *T* fields, with a maximum (9–10 m/s) in the equatorial region centered at 10°N and ~ 120 km.

The latitudinal structures of the terdiurnal tidal components Tw3, Ts0, and Tw1 have been presented in Figure 2 of *Du and Ward* [2010]. Here only the main features of these components are summarized. For the Tw3 *U* field, two maxima are symmetrically located in the middle/high latitudes of each hemisphere, centered at 40°–50°. The Tw3 *V* field has a broad region of significant amplitude ranging from 85°N to 85°S with three peaks (centered on 40°N, 10°N, and 50°S, respectively). Maximum amplitudes reach > 15 m/s above 110 km for both winds. The *T* field has significant amplitude from 80°N to 80°S with two maxima symmetrically located in the low and middle latitudes (10°–50°) of each hemisphere and centered at 30°–40°.

The maximum amplitudes increase with height and are <10 K below 110 km and increase to >15 K above 120 km.

For both the Ts0 and Tw1 *U* fields, there are maxima located in the polar regions with maximum amplitudes of 2–3 m/s and 5–8 m/s, respectively. The *V* field of Ts0 and Tw1 maximizes in the polar regions as well with maximum amplitudes of 4–5 m/s. For the Tw1 *T* field, the temperature amplitude remains significant from pole to pole above 100 km with peaks (2–4 K) in the polar regions, especially in the NPR. Ts0 maximizes at both poles with amplitudes of 6 K.

A significant number of components contribute to the tidal fields in the polar regions. Their structures and amplitudes vary. Tides which maximize within the polar regions include Dw1 winds above 100 km, Sw1 winds, and Ss0, Tw1, and Ts0 temperature and winds. Tidal components which maximize in nonpolar latitudes but have significant amplitudes in polar regions include De1, Ds0, and Se2 temperature and winds; Dw1, Sw1, Sw2, Sw3, and Tw3 temperature; and Dw1 winds below 100 km. A number of components maximize at the edge of the polar regions (50–60°N/S) and decrease in amplitude toward the pole. These include Sw2, Sw3, and Tw3 winds; Se1 temperature and winds; and Tw3 winds. Given these amplitude variations with latitude, the significant contributors to the tidal field in polar regions vary with latitude and are much more complex than the assumption made in earlier theoretical and observational studies that the winds have zonal wave number 1 structure and the temperatures zonal wave number 0 structure.

4. Seasonal Variability of the Polar Tides

Ground-based observations conducted in Antarctic and Arctic latitudes and in the height range of 80–100 km have shown that variability over a range of time scales (short-term, seasonal, and interannual variation) is typical. Of these, the seasonal variation is the most extensively discussed [*Forbes et al.*, 1995; *Baumgaertner et al.*, 2006; *Murphy et al.*, 2006; *Manson et al.*, 2009].

Seasonal variations of the significant polar tides identified from the model are presented as a function of height and month for the SPR and the NPR (Figures 3a–3d). The seasonal variation of tidal amplitudes is determined as the area-weighted mean over each polar region (this is a suitable measure since seasonal variations for a particular tide is similar throughout each polar region). The mean seasonal variation over the polar regions is calculated with amplitude information only. The temporal window for the seasonal variation plots is monthly mean. The discussion of the seasonal variation is undertaken using only the zonal wind field. The seasonal variations of the temperature and meridional wind are similar to those of the zonal wind, although their latitudinal structures can be very different. The four seasons in the NH are defined as spring (April–June), summer (July–September), autumn (October– December), and winter (January–March); the seasons in the SH are opposite to those of the NH; for example, the SH summer corresponds to the same months as the NH winter. Of particular note in this analysis is the hemispheric symmetry or asymmetry between the two polar regions (i.e., whether the component is enhanced in both hemispheres at the same time or same season).

Figure 3a shows the seasonal variations (height-month distributions) of the three diurnal tidal components (De1, Ds0, and Dw1) in the SPR and NPR. For the De1 component, there is hemispheric asymmetry between the polar regions. In both polar regions, the maximum amplitudes occur during the respective summer months. The SPR amplitude maximizes during summer (November–February) at the height range of 75–90 km and above 120 km. There is a secondary maximum during June and July in the height range of 100–110 km. The De1 component in the NPR also maximizes (mean amplitude of 6 m/s) during the summer months (May–August) below 100 km. There is a secondary maximum above 105 km during the winter (December to February), which matches the height range and time of its SPR counterpart.

For the Ds0 *U* field (Figure 3a, middle row), the maximum occurs symmetrically in both polar regions during May to September, with the maximum in the SPR being slightly stronger and lasting longer (into October). The area-weighted mean amplitude is 4–5 m/s. The temperature field (figures not shown) for this component is much stronger than the wind fields in the polar regions, with maximum amplitude greater than 10 K at 60°N/S.

The seasonal variation of the Dw1 polar zonal wind component is characterized by an annual variation with a maximum during April–October in the NPR and October–April in the SPR and hence has hemispheric asymmetry. This is in contrast to the well-known semiannual variation for the equatorial and low-latitude maxima associated with this component [*Burrage et al.*, 1995; *McLandress et al.*, 1996]. The area-weighted

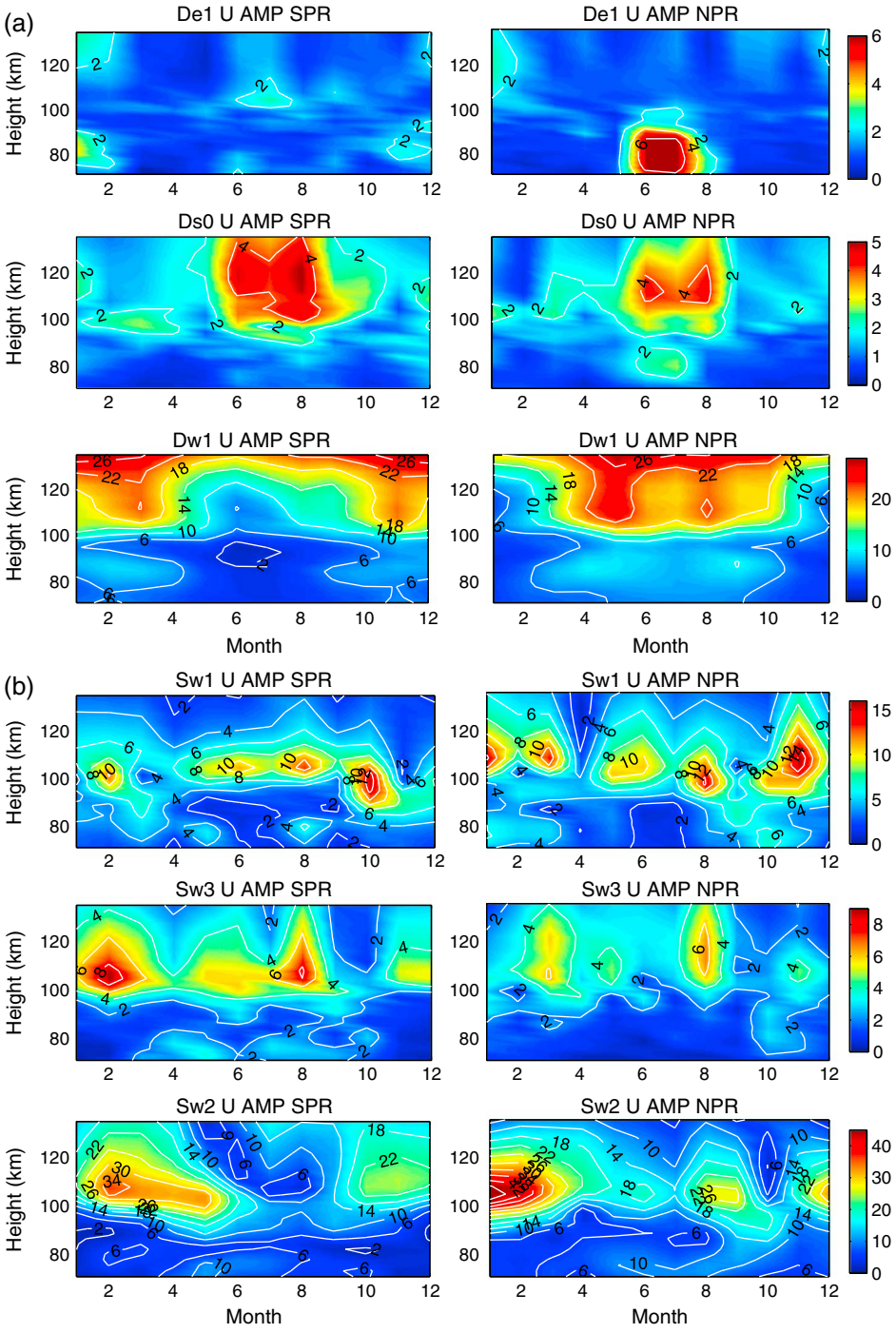

Figure 3. Seasonal variations of zonal wind (*U*) amplitude (m/s) for (a) De1, Ds0, and Dw1; (b) Sw1, Sw2, and Sw3; (c) Se1, Ss0, and Se2; and (d) Tw1, Ts0, and Tw3 over the Southern Polar Region (SPR) and the Northern Polar Region (NPR) from eCMAM. The height range is from 75 to 130 km and the amplitudes are area-weighted mean over each polar region.

maximum amplitude is over 25 m/s for both polar regions. Of note are the bimodal maxima associated with each hemisphere above 100 km (SPR: March and November; NPR: May and August).

Figures 3b and 3c present the polar seasonal variations of the semidiurnal tidal components (Sw1, Sw3, and Sw2 in Figure 3b and Se1, Ss0, and Se2 in Figure 3c). In contrast to the diurnal components, the semidiurnal components are quite variable with most components exhibiting several maxima during the year. *Du et al.* [2007]

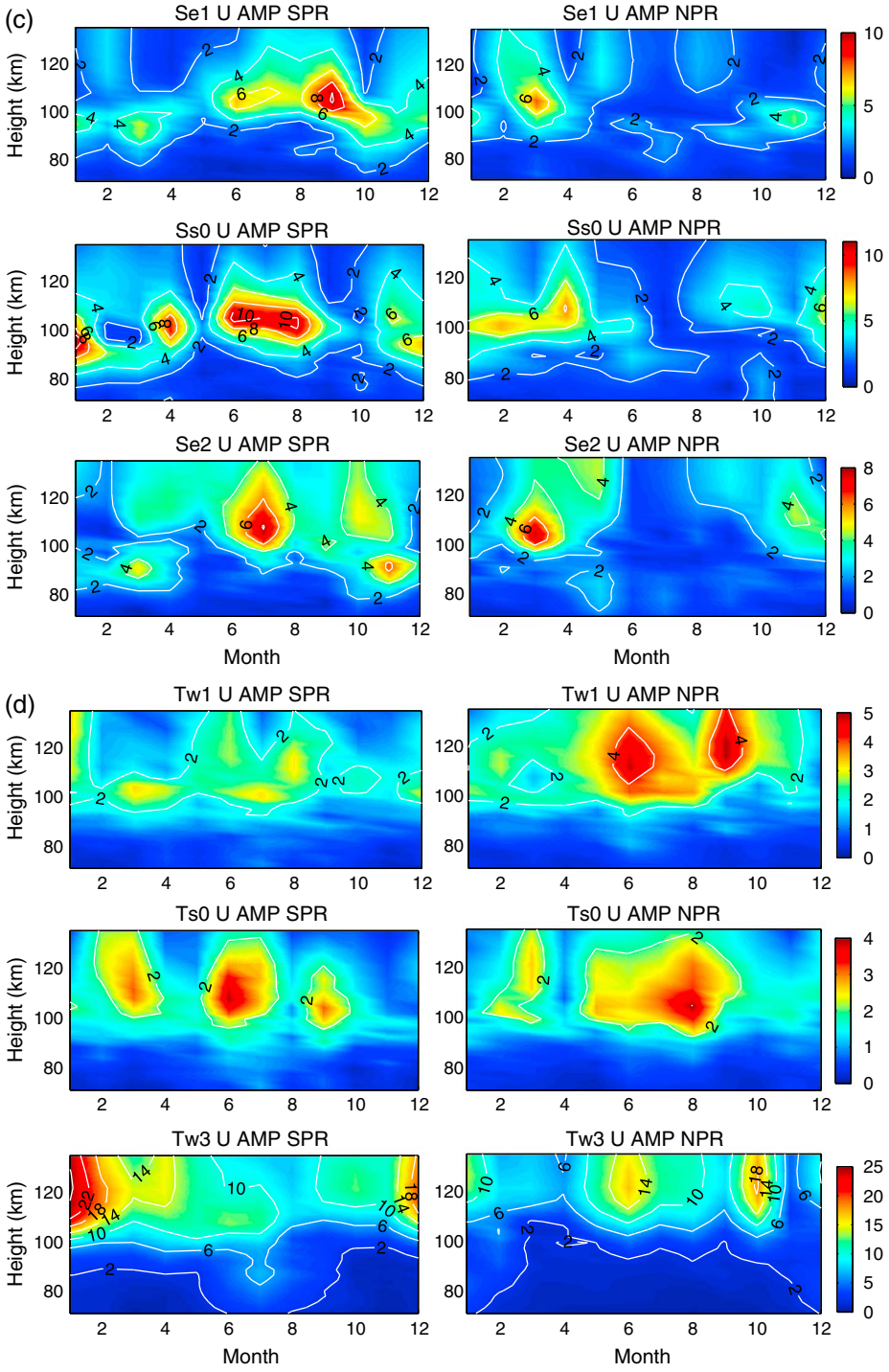

Figure 3. (continued)

compared the seasonal variations at 95 km between 45°S and 45°N of all the semidiurnal tidal components except Ss0 and Sw1 from eCMAM with TIDI/TIMED measurements. The polar seasonal behavior presented here differs from that noted for the equatorial and midlatitude region in *Du et al.* [2007] for most of the semidiurnal tidal components and the seasonal variations vary with height.

There are respectively four and five peaks in the SPR and NPR Sw1 *U* field during the year. The maxima during May–June and August coincide in time between the SPR and NPR. However, the timing of the other

maxima does not coincide with maximum in one hemisphere and minima in the other. Overall, the behavior is more symmetric during NH summer and asymmetric during NH winter. The strongest maximum in the SPR is located between 80 and 105 km during September–November with mean amplitude of over 15 m/s. Two secondary maxima are located above 100 km during April–September with mean amplitude of 10 m/s. There is also a local maximum centered in February and at 100 km with mean amplitudes of 8–10 m/s. The strongest maximum (mean of $>$ 15 m/s) in the NPR is present during October–December above 90 km with the amplitude maximizing at 110 km. NPR maxima corresponding to the SPR maxima occur in June and August at heights of 100 and 95 km and with maximum amplitudes of 10 and 12 m/s, respectively. Maxima also occur in January centered at ~ 110 km with mean amplitudes slightly greater than 10 m/s. April is the month with minimum amplitude for both polar regions.

For the seasonal variations of the Sw3 *U* field (Figure 3b, middle row), two strong maxima are seen in each polar region. In the SPR, they are centered on February and August, and in the NPR, they are centered on March and August. The maxima (6–8 m/s) in the SPR are stronger than those in the NPR (4–6 m/s). Two secondary maxima with amplitudes ~5 m/s are also present in each region and occur in June and December (May and November) in the SPR (NPR). The seasonal variation of this component is symmetric for the most part with maxima coinciding in time in both hemispheres.

The migrating semidiurnal tide, Sw2, is the strongest tidal component in the polar regions with zonal wind amplitudes that maximize above 35 m/s. In the SPR, the field varies annually with a minimum during NH summer months (the minimum broadens with height) and enhanced amplitude during October–April. It maximizes in February at 110 km with mean amplitude of ~35 m/s. The amplitude in the NPR remains significant throughout the year. It maximizes at 45 m/s in January at a height of 105 km and is significantly stronger than its SPR counterpart. A secondary maximum of 26 m/s occurs in August and local minima occur in July and October. The maxima in one hemisphere in general correspond to a minimum in the other so the amplitude variation for this component is asymmetric.

Figure 3c shows the seasonal variations of the semidiurnal components Se1, Ss0, and Se2 *U* fields. All are complex with several maxima during the year. In general, the response in the two polar regions is asymmetric. For the Se1 *U* field, the maximum in each polar region is present during the associated spring equinox: In the SPR, the maximum is centered on September and the maximum in the NPR is centered on March. The SPR maximum (8–10 m/s) has a longer duration and has stronger amplitude than the NPR maximum (6 m/s). There is a secondary maximum of similar amplitude (4 m/s) in both polar regions: The one in the SPR is centered on March and the one in the NPR is centered on November. The most striking feature in the Ss0 *U* field seasonal variation is the difference between the two polar regions. There are multiple peaks in the SPR and the most prominent maximum is present during May–September with mean amplitude of $>$ 10 m/s. There are also maxima centered on April and January with similar amplitude. The maximum amplitude in the NPR is much weaker (nearly half as large, ~6 m/s) than its SPR counterpart and mainly present during December–May.

The strongest maximum in the Se2 *U* field (Figure 3c, bottom row) in the SPR is present during June–August above 100 km and a secondary maximum occurs during October–December above 80 km. In the NPR, the strongest maximum is present during February–April above 95 km and the secondary maximum occurs in November. The maxima in both polar regions have similar mean amplitude of 4–8 m/s.

Figure 3d presents the three terdiurnal components in both polar regions: Tw1, Ts0, and Tw3. For the most part, amplitude variations in the two polar regions shadow each other (i.e., the temporal variations are parallel and hence symmetric) albeit with differing amplitudes. For the Tw1 *U* field, the maximum amplitude (4–5 m/s) in the NPR is much stronger than its southern counterpart (2–3 m/s). The primary maxima are present in June and September above 100 km with a secondary enhancement occurring in December/January. This component in the SPR maximizes at similar times although with smaller amplitudes (and the September maximum is less broad). The Ts0 field is somewhat similar in form to that of the Tw1 field. There are several maxima (coinciding in time in both polar regions). Maxima occur during the two equinoxes and during the NH summer solstice. The strongest maximum in the SPR is in May/June and the strongest maximum in the NPR is in August/September.

As with the other significant terdiurnal components, the seasonal variation of the migrating Tw3 *U* field (Figure 3c, bottom row) maximizes at similar times in both polar regions. The maximum (mean amplitude of 25 m/s) in the SPR occurs during December–February, and a secondary maximum (14 m/s) occurs in April.

Amplitudes of 6 m/s are seen during all months in the SPR above 100 km as is also the case for the NPR with the exception of November. The maximum in the NPR is much weaker than its southern counterpart. One maximum occurs in October with a mean amplitude of 14–18 m/s, and a secondary maxima (~14 m/s) occur in June and December/January.

Overall, three patterns of behavior of the amplitude variations are exhibited by these components. One pattern is that the seasonal variations coincide in time so that the seasonal signatures in both polar regions coincide (i.e., the temporal variations are the same in each hemisphere at the same time). An example of this seasonal behavior is Ds0, which maximizes during May–September in both polar regions. Other tidal components exhibiting the similar pattern include Tw1, Ts0, and Tw3 albeit with differing amplitudes in the two polar regions.

The second pattern is complementary to the first. The timing of the maxima in each polar region is shifted relative to each other by 6 months. The maxima in one hemisphere correspond to the minima in the other. When considered on a seasonal basis (taking into account the 6 month shift in seasons between hemispheres), the maxima coincide. An example of this seasonal variation pattern is the migrating diurnal tide Dw1: It maximizes in April–October in the NPR and in October–April in the SPR. The maximum amplitudes in the two polar regions coincide in season rather than time and are therefore out of phase by 180° between the two hemispheres for a particular month.

Most often, the seasonal variations in the two polar regions are the combinations of these two types of patterns albeit on a shorter time scale and depending on the individual month. This is the third pattern of variability. For certain months, the maxima coincide in time in both regions, and for other months, they are out of phase. The semidiurnal tide Sw1 has multiple peaks over an annual cycle at both polar regions. During the NH summer months, the timing and height of the maxima in each polar region coincide (first pattern), whereas between September and April, the times of the maxima in one hemisphere correspond to minima in the other (second pattern).

These patterns of variability can be interpreted in terms of Hough modes. Hough modes are orthogonal functions which arise naturally when solving the Laplace tidal equations for a windless, isothermal atmosphere [*Chapman and Lindzen,* 1970] and remain relevant for describing the form of components in realistic situations [*Forbes*, 1985]. Although the phase of these modes may be symmetric or antisymmetric across the equator, this cannot be seen from the amplitudes alone, which appear with the same values on either side of the equator. As a result, any single mode would appear to have similar amplitudes at both poles in Figures 1–3, irrespective of whether it is symmetric or antisymmetric. Tidal components that have amplitudes which differ significantly between the two poles at the same time must be composed of at least two modes, one symmetric and the other antisymmetric, so that in one polar region, constructive interference would result and in the other destructive interference would result.

For the first pattern (maxima at the same time in both polar regions), one or more modes of the same symmetry must be present (opposite symmetries would result in differing amplitudes in the two regions). These modes are modulated seasonally and the amplitude modulation in both hemispheres is concurrent.

The second pattern (maxima occurring in one polar region at the same time as minima in the other region) requires the presence of symmetric and antisymmetric modes of similar amplitude. In this case in one polar region, the modes would be in phase and interfere constructively so that the tidal amplitude would be large. In the other hemisphere, opposite circumstances would apply, the modes would interfere destructively, and the tidal amplitude would be small. The relative phasing of the symmetric and antisymmetric modes would alternate with season so that polar regions with constructive (destructive) interference would change seasonally.

The third pattern involves combinations of these two patterns but with seasonal variations in the mode composition and variability in the phasing and amplitudes of the modes occurring on a shorter than seasonal time scale. For the Sw1 component mentioned above, during NH hemisphere summer, modes of the same symmetry would be present and their amplitudes modulated on an approximately monthly time scale. During the rest of the year, symmetric and antisymmetric components are present so that the amplitude variation in each polar region is out of phase. The relative phase and amplitudes would be modulated on an approximately monthly time scale.

In the literature, variations in the latitudinal form of tidal modes as a result of dissipation and non-ideal conditions have been analyzed (under the terminology of mode coupling or generalized Hough modes) as an explanation for deviations in the observed latitudinal structure away from the Hough modes [see *Ortland*, 2005 and references therein]. However, these deviations are not substantial enough to eliminate amplitudes in one hemisphere and the modified latitude structure remains close to symmetric about the equator. Hence, the effects of dissipation and non-ideal conditions are unlikely to explain the strong variability of components observed in this model run.

An examination of the cause(s) of this behavior requires careful study of the modal structure of these components and their excitation. Seasonal variations in the forcing of these components would be expected from the seasonal variation in the latitudinal distribution in solar heating. This variation in heating will result in the preferential excitation of different components as a function of season. Dissipation associated with the background wind and temperature fields and other source mechanisms will also need to be taken into account. Further understanding of the behaviors corresponding to different tidal components is beyond the scope of this paper and will be pursued in a future study involving a detailed Hough mode decomposition analysis.

5. Statistical Correlations Between Tides and SPW1 in eCMAM

One often proposed source for nonmigrating tides is nonlinear interactions. In such an interaction, two interacting parent waves generate child waves that have frequencies and wave numbers equal to the sum and difference of those of the parent waves [*Teitelbaum and Vial*, 1991]. In accordance with this theory, interactions between the migrating Sw2 (Dw1) and the SPW1 have been proposed as a possible source for the nonmigrating Sw1 (Ds0) and Sw3 (Dw2) tides. Time series of the amplitudes of these waves diagnosed from this eCMAM run provide a means of examining the viability of these interactions in the model. Correlations between these components are used to explore the extent to which these interactions occur.

Strong and positive statistical correlations between the child nonmigrating tides and SPW1 in the opposite winter hemisphere have been interpreted as evidence for nonlinear interaction between the migrating tides and SPW1 [*Baumgaertner et al.*, 2006; *Murphy et al.*, 2009; *Smith et al.*, 2007; *Xu et al.*, 2009; *Chang et al.*, 2009]. The amplitude of the migrating tides is noted to be anticorrelated with that of SPW1 and the child nonmigrating tides, indicating energy loss to the child waves [*Palo et al.*, 1998; *Norton and Thuburn*, 1999; *Chang et al.*, 2009]. The observation community in the Antarctic has demonstrated positive correlations between the observed SH Sw1 in the MLT region and the NH SPW1 in the stratosphere (derived from satellite or model assimilated data) [*Baumgaertner et al.*, 2006; *Murphy et al.*, 2009]. In the Arctic, *Smith et al.* [2007] found a correlation between variability of the mesospheric semidiurnal tide at Esrange (68°N, 21°E) and the amplitude of SPW1 in the SH stratosphere and lower mesosphere during NH summer and fall. However, using radar observations at Saskatoon (52°N, 253°E), Tromsø (70°N, 19°E), Collm (51°N, 13°E), Eureka (80°N, 86°W), and Svalbard (78°N, 16°E), *Xu et al.* [2009] noted that the nonmigrating semidiurnal tides observed at NH high/Arctic latitudes failed to exhibit any real correlation with the Antarctic SPW1 during NH summer-fall and raised questions with respect to these proposed inter-hemispheric SPW-tide physical links. In the same paper, *Xu et al.* [2009] used cross-spectral analysis to show that the strong correlations found between tides in the SH Antarctic latitudes and the NH SPW1 were primarily associated with the low-frequency fluctuations ($>$15 days) and queried what the time scales of the correlations found in prior work were.

Another approach to study nonlinear interaction is to use realistic models in which the parent waves could be turned on or off. Using this approach, *Angelats i Coll and Forbes* [2002] were able to generate the observed summertime high-latitude enhancement of the Sw1 in a spectral model, as a by-product of nonlinear interactions between the migrating Sw2 and a prescribed SPW1 profile in the winter hemisphere stratosphere and lower mesosphere. Modeling studies by *Yamashita et al.* [2002] and *Aso* [2007] were also able to provide evidence for the presence of these nonlinear interactions. A recent modeling study by *Chang et al.* [2009] found that the short-term variability of the Sw1 during the 2002 SH stratospheric sudden warming (SSW) in Thermosphere-Ionosphere-Mesosphere-Electrodynamics General Circulation Model (TIME-GCM) is strongly dependent upon the SPW1 events prior to the major warming. Despite the above studies, it was also noted that the global distribution of the Sw1 in the lower thermosphere showed a strong sensitivity to the background zonal mean wind profile [*Yamashita et al.*, 2002] and the planetary

wave-induced changes in the background atmosphere can drive tidal variability at levels greater than those attributed to nonlinear interaction [*Chang et al.*, 2011].

Proving the existence of nonlinear interactions is difficult especially with observations. The presence of local correlations between components is only part of this proof. Correlations without other supporting evidence do not constitute proof of any particular cause. For example, unless proven otherwise, correlations could be due to variations associated with a common source or common filtering effects away from the region where correlations are observed.

In this section, global statistical correlations between appropriate waves in eCMAM are calculated in order to identify whether amplitude variations in parent/child waves can be attributed to nonlinear interactions. Following *Du and Ward* [2010], correlations are examined using two time series involving different time scales under the assumption that nonlinear interactions should appear on all scales. Significance tests of the correlations are done with a Gaussian random model (uncorrelated white noise) based on the individual characteristics of the two filtered time series. Mathematical derivations show that a Gaussian random model has to be based on the original time series and undergo the same filtering process as the original time series in order to obtain correct significance test on the filtered time series (for details refer to Text S1 in the supporting information). The equation $c_m = \sqrt{2/m}$ is a very good approximation of the 95% confidence limits of filtered data using Fourier transform for $m \geq 10$, where m is numbers of unfiltered wavelengths. If significance tests are undertaken on a subset of the original time series using statistics based on the full time series, then the threshold for significance will be higher than calculated from the above equation.

Two groups of proposed parent-child tides are examined in this paper:

1. Dw1 + SPW1 (Parent waves) → Dw2 + Ds0 (Child waves)
2. Sw2 + SPW1 (Parent waves) → Sw1 + Sw3 (Child waves)

Both the tidal and the SPW1 amplitudes relevant to the candidate parent/child waves were diagnosed using a sliding 4 day window stepped by 2 days to provide suitable time series. While the relatively short averaging window used for SPW1 will result in aliasing with longer-period planetary waves, it was deemed necessary in order to examine the variability of the SPW and the tide on shorter time scales. Time series for tides are taken from the zonal wind field, and the SPW1 time series are from the geopotential height field. The SPW1 time series tends to maximize at 60°N(S), 50 km and their temporal variations are very similar within the stratosphere and lower mesosphere during NH (SH) winter (figure not shown). Therefore, we use the SPW1 time series at 60°N(S) and 50 km as the representation of SPW1 in the stratosphere and lower mesosphere. The correlations are calculated at two time periods: October–March (SPW1 maximizes in NH) and April–September (SPW1 maximizes in SH) for the original time series, a low-pass-filtered time series (LPFTS) and the high-pass-filtered time series (HPFTS), respectively. The filter cutoff is chosen as 18 days (in accordance with the 15 days suggested in *Xu et al.* [2009]) and applied to both the assumed parent and child waves to obtain the long-term (e.g., LPFTS) and short-term variation time series (e.g., HPFTS). Significant temporal variability is seen for the original time series, the LPFTS and HPFTS associated with all waves (figure not shown).

The correlations are presented in Figures 4 (diurnal tides) and 5 (semidiurnal tides). White spaces indicate regions where the correlation is below the 95% significance level. These correlations are interpreted in the following way. First, we expect nonlinear interactions to be present on short time scales. In addition, in accordance with the literature, energy is expected to flow from one of the parent waves (in the literature this is identified as the tidal parent wave not the planetary wave) to the child waves. As a result we would expect the tidal (planetary) parent wave and child waves to be negatively (positively) correlated with each other and the two child waves to be positively correlated (i.e., the amplitude of one parent wave would decrease and at the same time the amplitudes of the child waves would increase). We examine whether these correlations exist globally and between the original time series, the LPFTS and the HPFTS.

5.1. Correlations Among Ds0, Dw2, Dw1, and SPW1

Figure 4a shows the latitude-height cross section of correlation coefficients during April–September for Dw2/Ds0 versus SPW1 at 60°S and 50 km. The left panels of Figure 4a are correlations of Dw2 versus SH SPW1 for the original time series–total variability (top), the LPFTS-variability $>$ 18 days (middle), and the HPFTS-variability $<$ 18 days (bottom). The right column of Figure 4a are similar to the left column but

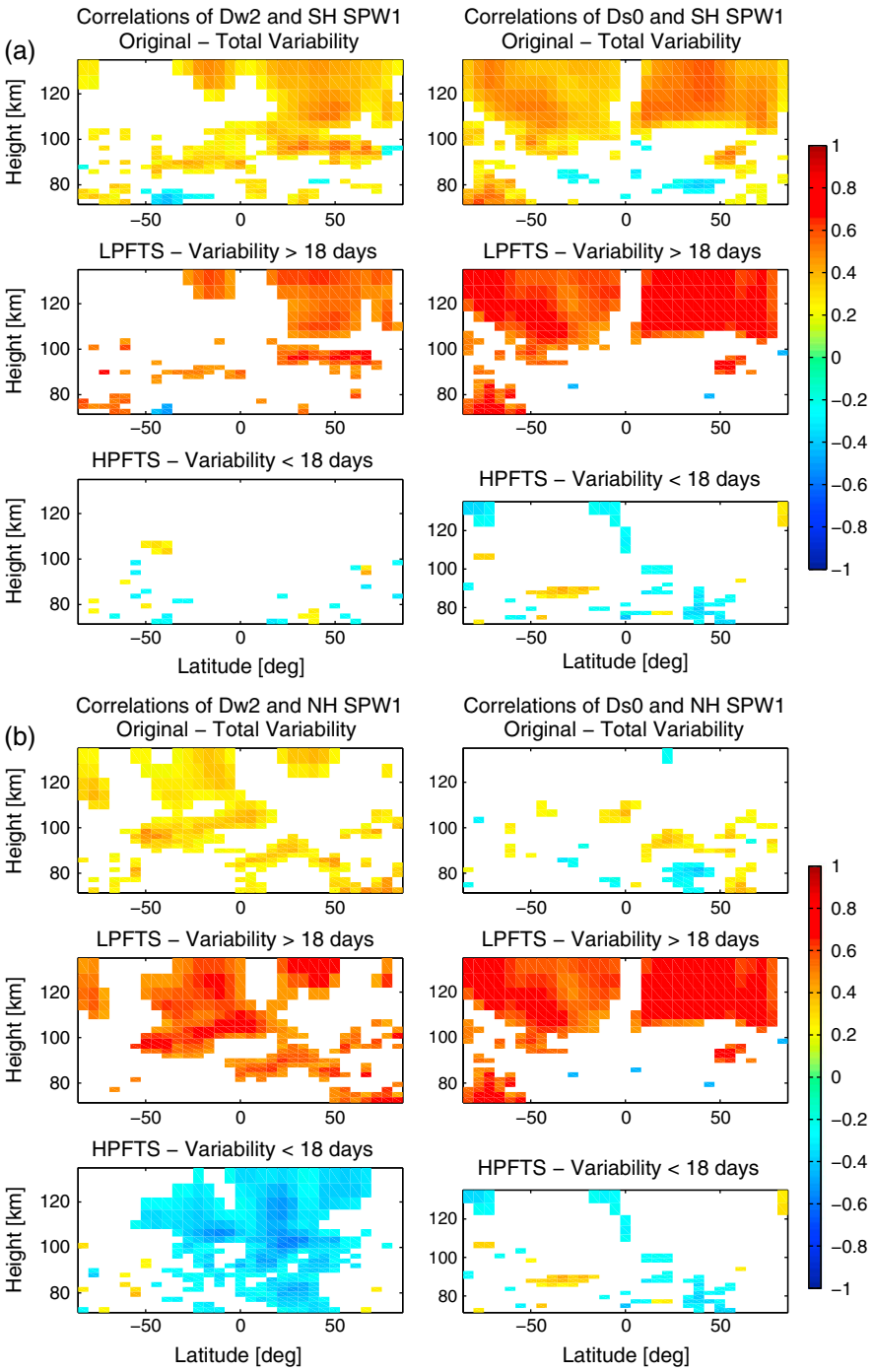

Figure 4. (a) Correlation coefficients of the original time series–total variability, LPFTS-variability > 18 days, and HPFTS-variability 18 days of Dw2 versus SPW1 at 60°S, 50 km and Ds0 versus SPW1 at 60°S, 50 km for April–September. (b) Similar as Figure 4a but with SPW1 at 60°N, 50 km, and during October–March. White areas indicate confidence level less than 95%.

for the correlations of Ds0 versus SH SPW1. Figure 4b is similar to Figure 4a but presents the correlations during October–March for Dw2/Ds0 versus SPW1 at 60°N and 50 km.

For the original time series between Dw2 and the SH SPW1 during April–September (Figure 4a, left column, top plot), the correlations are strong and positive extending from the SH MLT high latitude across the equator into the lower thermosphere of the NH. This is consistent with previous hypotheses of the nonlinear

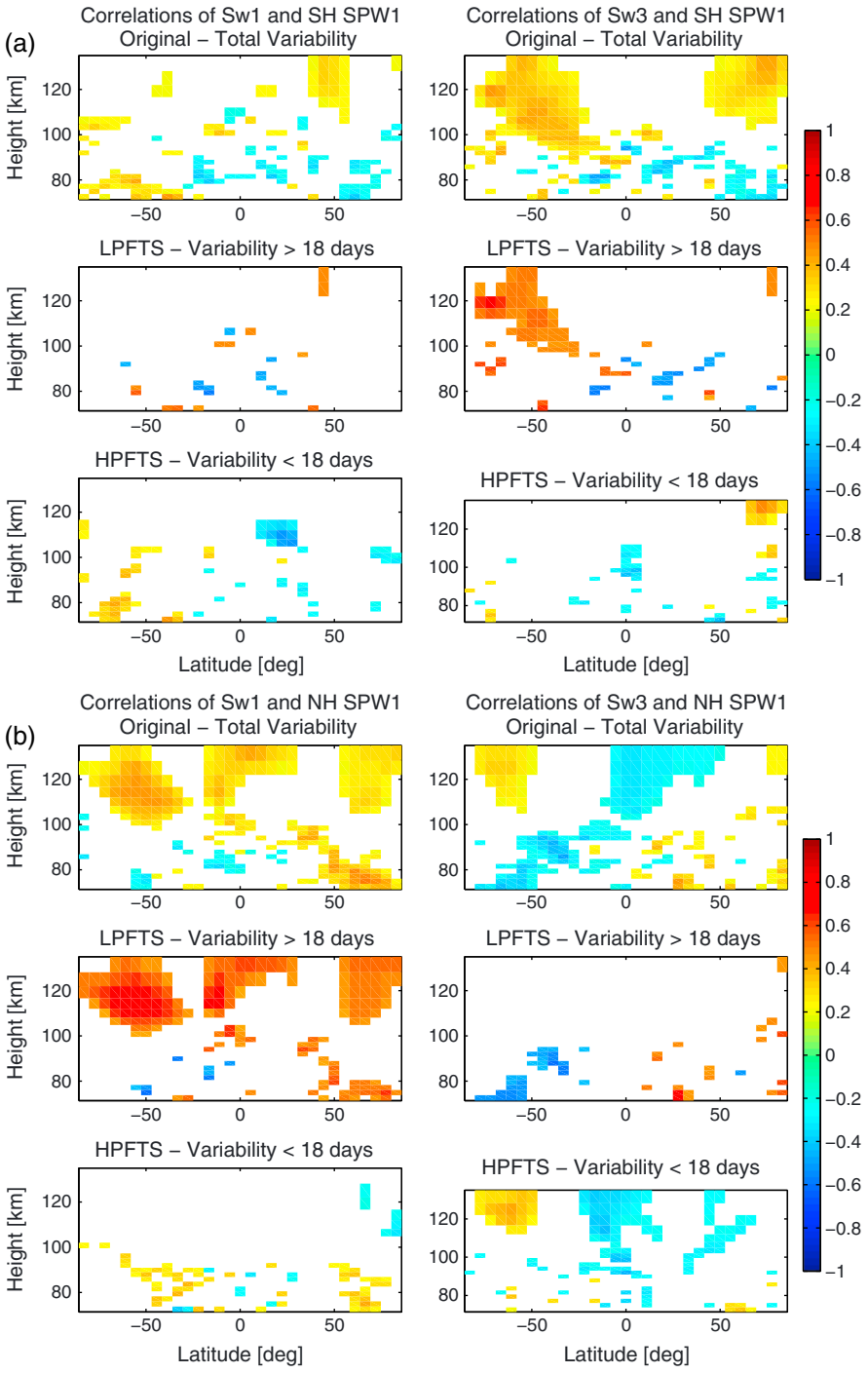

Figure 5. (a) Correlation coefficients of the original time series–total variability, LPFTS-variability > 18 days, and HPFTS-variability < 18 days of Sw1 versus SPW1 at 60°S, 50 km and Sw3 versus SPW1 at 60°S, 50 km for April–September. (b) Similar as Figure 5a but with SPW1 at 60°N, 50 km, and during October–March. White areas indicate confidence level less than 95%.

interactions in the opposite hemispheres and transhemispheric propagation which result in positive correlations between the child wave and the SPWs activity [*Chang et al.*, 2009]. However, the strong positive correlations seen in the original time series only exist for the LPFTS-variability > 18 days (left panel, middle plot) but disappear for the HPFTS-variability < 18 days (left panel, bottom plot).

For the original time series between Ds0 and the SH SPW1 during April–September (Figure 4a, right column, top plot), the correlations are strong and positive in both hemispheres above 100 km. As with Dw2, the strong and positive correlations are only present for the LPFTS-variability $>$ 18 days (right panel, middle plot) but absent for the HPFTS-variability $<$ 18 days (right panel, bottom plot).

Correlations of the two assumed parent waves—the Dw1 and SPW1—are also calculated during April–September (figures not shown). The original time series of the two waves are mostly anticorrelated over a broad region between 50°N and 60°S and below 100 km. This anticorrelation between the migrating Dw1 and the SPW1 is consistent with previous work [*Palo et al.*, 1998; *Norton and Thuburn*, 1999; *Chang et al.*, 2009]. However, these strong negative correlations again are only present for the LPFTS-variability $>$ 18 days but absent for the HPFTS-variability $<$ 18 days, which suggests that the strong negative correlations mainly come from the longer-term variability of the time series.

The correlations between the two assumed child nonmigrating tides Dw2/Ds0 and the migrating tide Dw1 are also calculated during April–September (figures not shown). Previous studies suggested that Dw1 nonlinearly interacts with the SPW1 and, as a result, loses energy to the child waves Dw2 and Ds0. Negative correlations would be expected between the child wave and the migrating tide [*Palo et al.*, 1998; *Norton and Thuburn*, 1999; *Chang et al.*, 2009]. The original time series (total variability) of the Dw2 and Dw1 are positively correlated at some locations and the HPFTS are negatively correlated at some locations. However, the locations of positive correlations do not coincide with the locations of negative correlations and these correlations show little coherence in height and latitude. Local correlations can be significant for a single location over short periods of time but there does not appear to be global significance to these correlations.

The total variations between the Dw1 and Ds0 are mainly positively correlated below 100 km and negatively correlated above 100 km during April–September. However, these correlations are generally not significant for the HPFTS-variability $<$ 18 days.

While the form of the correlations of this group of waves in October–March (Figure 4b) differs from that diagnosed in April–September, similar conclusions can be drawn. The original time series of Dw2 in the SH MLT region are positively correlated with the NH SPW1 in the stratosphere and lower mesosphere (Figure 4b, left column, top plot). The positive correlations seen in the original time series are mainly due to the LPFTS-variability $>$ 18 days (left column, middle plot), while their HPFTS-variability $<$ 18 days is mostly negatively correlated (left column, bottom plot).

There are no significant correlations of a global extent for both the original time series and HPFTS between Ds0 and NH SPW1 in October–March (Figure 4b, right column, top and bottom plots). As in April–September, although the Dw1 and NH SPW1 original time series are negatively correlated over a broad region, these correlations are not significant for the HPFTS (figures not shown). The correlations between Dw2 and Dw1 in October–March are not significant for the original time series at most of the locations. No significant correlations are seen for both original time series and HPFTS between Ds0 and Dw1 in October–March (figures not shown).

From the above correlation analysis, hemispheric differences are obvious. Overall, the correlations with the original times series among this group of waves tend to be stronger for those involving the SH SPW1 during April–September. This is especially the case for Ds0 and SPW1. The correlations are strong and positive between the original time series in both hemispheres of the MLT region during April–September. However, the correlations are not significant during October–March when the SPW1 is strong in the NH. Also of importance is the fact that the correlations are very time scale dependent. The strong correlations seen with the original time series are generally not present for the HPFTS-variability $<$ 18 days. At times, the correlations are of opposite sign for the two time series (e.g., Dw2 and NH SPW1 original and HPFTS).

5.2. Correlations Among Sw1, Sw3, Sw2, and SPW1

The second set of waves often considered to be related through nonlinear interactions involves the migrating semidiurnal tide Sw2 interacting with the SPW1 to generate the nonmigrating semidiurnal tides Sw3 and Sw1. A similar correlation analysis as above is undertaken to examine the nature of the interaction between these waves. These correlations are presented in Figure 5 in the same manner as Figure 4. Figure 5a is for the period of April–September and Figure 5b for October–March.

For April–September, the correlations of the original time series, LPFTS, and HPFTS between Sw1 and SPW1 are not globally significant (Figure 5a, left column). In contrast, for October–March, the original time series of Sw1 in the MLT region is positively correlated with the SPW1 above 100 km (Figure 5b, left column, top plot). However, these correlations are mainly due to LPFTS-variability $>$ 18 days (Figure 5b, left column, middle plot) and disappear when the two HPFTS are considered (Figure 5b, left column, bottom plot).

There are strong correlations between the original time series of Sw3 and SPW1 in the high latitudes above 100 km during April–September (Figure 5a, right column, top plot). However, these strong positive correlations are absent for the associated HPFTS (Figure 5a, right column, bottom plot). During October–March, the correlation of Sw3 with the SPW1 is positive in the SH high latitudes and negative in the equatorial region above 100 km, for both the total time series and HPFTS (Figure 5b, right column, top and bottom plots). There are no significant correlations for the LPFTS-variability $>$ 18 days (Figure 5b, right column, middle plot). This is the only component and time period for which strong positive correlations with SPW1 exist for both total time series and HPFTS. However, no coherent correlations are present between the other waves during the same period.

The time series of the two assumed parent waves—the Sw2 and the SPW1—are generally anticorrelated in the SH and positively correlated in the NH above 100 km during both time periods. The SH negative correlations are stronger during April–September than October–March and the NH positive correlations are stronger during October–March than April–September. However, similar strong correlations for the associated HPFTS are absent and not global in extent (figures not shown).

The total time series of the Sw2 and Sw1/Sw3 are generally positively correlated in the NH high latitudes during April–September; however, these positive correlations are absent for the HPFTS (figures not shown). The total time series of Sw2 and Sw3 are negatively correlated in the SH above 100 km during April–September but are not significant at most locations for the HPFTS (figures not shown). For the period of October–March, the correlations between Sw2 and Sw1/Sw3 for both the total time series and HPFTS are not significant at most locations. There is little coherence in height and latitude, and hence, the correlations are not globally significant for both sets of time series (figures not shown).

Again, the correlations are very time scale dependent. The strong correlations in the original time series are mainly found in the longer-term variations ($>$18 days) but not in the short-term variations ($<$18 days). These strong long-term correlations are most likely associated with the large-scale seasonal variations in the sources and propagation characteristics of the various waves.

6. Conclusions

The eCMAM is used to study the characteristics of the polar tides (diurnal, semidiurnal, and terdiurnal) in the MLT region. The latitudinal structures of the annual mean amplitudes of significant polar tidal components are presented for the temperature (*T*), zonal wind (*U*), and meridional wind (*V*) fields. Their seasonal variations are discussed using the associated zonal wind field. The model results reveal strong seasonal, latitude, and altitude variations and interhemispheric symmetry/asymmetry for these components.

The most significant diurnal, semidiurnal, and terdiurnal tides in the polar regions in this model run are Ds0, Dw1, and De1; Sw3, Sw2, Sw1, Ss0, Se1, and Se2; and Tw3, Ts0, and Tw1, respectively. Of note is the existence of a strong nonmigrating De3 feature in the SPR between 70 and 90 km, which is not seen in the NPR. Components which contribute significantly to polar tidal amplitudes include those which maximize in polar regions (Dw1 above 100 km, Sw1 U V, Sw2 U V, Ss0, Se1, Tw3 U V, Ts0, and Tw1) and those which maximize at nonpolar latitudes but still have significant amplitudes in polar regions (De1, Ds0, Sw1 T, Sw2 T, Sw3, Se2, and Tw3).

All the above tidal components exhibit significant seasonal variations. Some of the tidal components maximize during the same season in both polar regions. For example, the migrating diurnal tide Dw1 in the NPR maximizes between April and October and it maximizes in the SPR between October and April. Another group of components maximizes at the same time (but opposite season) in both polar regions. Ds0, which maximizes during May–September in both polar regions is an example of this behavior. A number of other components have amplitude variations on a shorter than seasonal time scale with the amplitude variations exhibiting a mixture of the above two scenarios. For example, the nonmigrating semidiurnal tide Sw1 has multiple peaks

over an annual cycle in both polar regions. At times, the amplitudes maximize at the same time, whereas during other periods, they are complementary in time with maximum amplitude occurring in one hemisphere or the other. Further study of the sources for these components is needed to provide insight into the differences in interhemispheric symmetries/asymmetries exhibited by the various components.

One potential generation mechanism for the nonmigrating tides, namely, nonlinear interactions between the migrating tides and the SPW1, is examined using systematic global correlation analysis. This problem is approached by first examining correlations between total time series of the relevant components and comparing them to the correlations between the associated LPFTS and HPFTS. The results indicate that the correlations are highly time scale dependent. The significant correlations are mainly due to the longer-term variations ($>$18 days) and no global significant correlations are found for the short-term variations ($<$18 days). Studies of satellite observations which provide similar global correlation analyses are important (although difficult with currently available mission) to determine whether these model analyses are authentic representations of the real atmosphere or not (in which case further improvements to the models is needed).

Acknowledgments

The authors wish to acknowledge Tom Flannaghan and Alison Ming from University of Cambridge for their inputs and discussion of the significance test. Jian Du was funded by the U.S. Department of Energy grant DE-SC0005473, NSF CEDAR grant AGS-1243019, and the Canadian Foundation for Climate and Atmospheric Science (CFCAS) as part of the scientific analysis effort of the Polar Environment Atmospheric Research Laboratory (PEARL). Other CABDAC/PEARL funding partners are: the Arctic Research Infrastructure Fund, Atlantic Innovation Fund/Nova Scotia Research Innovation Trust, Canadian Foundation for Innovation, Canadian Space Agency, Environment Canada, Government of Canada International Polar Year, NSERC, Ontario Innovation Trust, Ontario Research Fund, Indian and Northern Affairs Canada, and the Polar Continental Shelf Program. William Ward was supported by the Natural Sciences and Engineering Council (NSERC) and CFCAS. Fenwick Cooper was supported by Natural Environment Research Council (NERC) grant NE/G003122/1.

References

Akmaev, R. A. (2001), Seasonal variations of the terdiurnal tide in the mesosphere and lower thermosphere: A model study, *Geophys. Res. Lett.*, *28*, 3817–3820, doi:10.1029/2001GL013002.

Angelats i Coll, M., and J. M. Forbes (2002), Nonlinear interactions in the upper atmosphere: The $s=1$ and $s=3$ nonmigrating semidiurnal tides, *J. Geophys. Res.*, *107*(A8), 1157, doi:10.1029/2001JA900179.

Aso, T. (2003), An overview of the terdiurnal tide observed by polar radars and optics, *Adv. Polar Upper Atmos. Res.*, *17*, 167–176.

Aso, T. (2007), A note on the semidiurnal non-migrating tide at polar latitudes, *Earth Planets Space*, *59*, e21–e24.

Baumgaertner, A. J. G., A. J. McDonald, G. J. Fraser, and G. E. Plank (2005), Long- term observations of mean winds and tides in the upper mesosphere and lower thermosphere above Scott Base, Antarctica, *J. Atmos. Sol. Terr. Phys.*, *67*(16), 1480–1496.

Baumgaertner, A. J. G., M. J. Jarvis, A. J. McDonald, and G. J. Fraser (2006), Observations of the wave number 1 and 2 components of the semidiurnal tide over Antarctica, *J. Atmos. Sol. Terr. Phys.*, *68*(11), 1195–1214.

Beagley, S. R., C. McLandress, V. I. Fomichev, and W. E. Ward (2000), The extended Canadian Middle Atmosphere Model, *Geophys. Res. Lett.*, *27*, 2529–2532, doi:10.1029/1999GL011233.

Burrage, M. D., M. E. Hagan, W. R. Skinner, D. L. Wu, and P. B. Hays (1995), Long-term variability in the solar diurnal tide observed by HRDI and simulated by the GSWM, *Geophys. Res. Lett.*, *22*, 2641–2644, doi:10.1029/95GL02635.

Chang, L. C., S. E. Palo, and H.-L. Liu (2009), Short-term variation of the $s=1$ nonmigrating semidiurnal tide during the 2002 stratospheric sudden warming, *J. Geophys. Res.*, *114*, D03109, doi:10.1029/2008JD010886.

Chang, L. C., S. E. Palo, and H.-L. Liu (2011), Short-term variability in the migrating diurnal tide caused by interactions with the quasi 2 day wave, *J. Geophys. Res.*, *116*, D12112, doi:10.1029/2010JD014996.

Chang, L. C., et al. (2012), Comparison of diurnal tide in models and ground-based observations during the 2005 Equinox CAWSES Tidal Campaign, *J. Atmos. Sol. Terr. Phys.*, *78–79*, 19–30, doi:10.1016/j.jastp.2010.12.010.

Chapman, S., and R. S. Lindzen (1970), *Atmospheric Tides*, D. Reidel Co., Hingham, Mass.

Davis, R. N., J. Du, A. K. Smith, N. J. Mitchell, and W. E. Ward (2013), The diurnal and semidiurnal tides in the tropical mesosphere over Ascension Island (8S, 14W) and their interaction with the stratospheric quasi-biennial oscillation: Studies with meteor radar, eCMAM and WACCM, *Atmos. Chem. Phys.*, *13*, 9543–9564, doi:10.5194/acp-13-9543-2013.

Du, J. (2008), A mesosphere and lower thermosphere dynamics study using the extended Canadian Middle Atmosphere Model (CMAM), PhD thesis, Univ. of New Brunswick, Canada.

Du, J., and W. E. Ward (2010), Terdiurnal tide in the extended Canadian Middle Atmospheric Model (CMAM), *J. Geophys. Res.*, *115*, D24106, doi:10.1029/2010JD014479.

Du, J., W. E. Ward, J. Oberheide, T. Nakamura, and T. Tsuda (2007), Semidiurnal tides from the Extended Canadian Middle Atmosphere Model (CMAM) and comparisons with TIMED Doppler Interferometer (TIDI) and meter radar observations, *J. Atmos. Sol. Terr. Phys.*, *69*, 2159–2202, doi:10.1016/j.jastp.2007.07.014.

Fisher, G. M., R. J. Niciejewski, T. L. Killeen, W. A. Gault, G. G. Shepherd, S. Brown, and Q. Wu (2002), Twelve hour tides in the winter northern polar mesosphere and lower thermosphere, *J. Geophys. Res.*, *107*(A8), 1211, doi:10.1029/2001JA000294.

Fomichev, V. I., W. E. Ward, S. R. Beagley, C. McLandress, J. C. McConnell, N. A. McFarlane, and T. G. Shepherd (2002), Extended Canadian Middle Atmosphere Model: Zonal-mean climatology and physical parameterizations, *J. Geophys. Res.*, *107*(D10), 4087, doi:10.1029/2001JD000479.

Forbes, J. M. (1985), Middle atmosphere tides, *J. Atmos. Terr. Phys.*, *46*, 1049–1067.

Forbes, J. M., and D. Wu (2006), Solar tides as revealed by measurements of mesosphere temperature by the MLS experiment on UARS, *J. Atmos. Sci.*, *63*(7), 1776–1797.

Forbes, J. M., N. A. Makarov, and Y. Portnyagin (1995), First results from the meteor radar at South Pole—A large 12-hour oscillation with zonal wave-number one, *Geophys. Res. Lett.*, *22*, 3247–3250.

Forbes, J. M., S. E. Palo, and F. A. Marcos (1999), Longitudinal structures in lower thermosphere density, *J. Geophys. Res.*, *104*, 4373–4385.

Fraser, G. J., Y. I. Portnyagin, J. M. Forbes, R. A. Vincent, I. A. Lysenko, and N. A. Makarov (1995), Diurnal tide in the Antarctic and Arctic mesosphere/lower thermosphere regions, *J. Atmos. Terr. Phys.*, *57*, 383–393.

Hagan, M. E., and J. M. Forbes (2003), Migrating and nonmigrating semidiurnal tides in the upper atmosphere excited by tropospheric latent heat release, *J. Geophys. Res.*, *108*(A2), 1062, doi:10.1029/2002JA009466.

Hagan, M. E., and R. G. Roble (2001), Modeling diurnal tidal variability with the NCAR TIME-GCM, *J. Geophys. Res.*, *106*, 24,869–24,882.

Hernandez, G., R. W. Smith, G. J. Fraser, and W. L. Jones (1992a), Large-scale waves in the upper mesosphere at Antarctic high latitudes, *Geophys. Res. Lett.*, *19*, 1347–1350.

Hernandez, G., R. W. Smith, and J. F. Conner (1992b), Neutral wind and temperature in the upper mesosphere above South Pole, Antarctica, *Geophys. Res. Lett.*, *19*, 53–56.

Hernandez, G., G. J. Fraser, and R. W. Smith (1993), Mesospheric 12-hour oscillation near South Pole, Antarctica, *Geophys. Res. Lett.*, *20*, 1787–1790.
Hernandez, G., R. W. Smith, and G. J. Fraser (1995), Antarctic high-latitude mesospheric dynamics, *Adv. Space Res.*, *16*(5), 71–80.
Hines, C. O. (1997a), Doppler spread parameterization of gravity wave momentum deposition in the middle atmosphere. Part 1. Basic formulation, *J. Atmos. Sol. Terr. Phys.*, *59*, 371–386, doi:10.1016/S1364-6826(96)00079-X.
Hines, C. O. (1997b), Doppler spread parameterization of gravity wave momentum deposition in the middle atmosphere. Part 2. Broad and quasi-monochromatic spectra, and implementation, *J. Atmos. Sol. Terr. Phys.*, *59*, 387–400, doi:10.1016/S1364-6826(96)00080-6.
Hocking, W. K. (2001), Middle atmosphere dynamical studies at Resolute Bay over a full representative year: Mean winds, tides, and special oscillations, *Radio Sci.*, *36*, 1795–1822, doi:10.1029/2000RS001003.
Hoffmann, P., W. Singer, D. Keuer, W. K. Hocking, M. Kunze, and Y. Murayama (2007), Latitudinal and longitudinal variability of mesospheric winds and temperatures during stratospheric warming events, *J. Atmos. Sol. Terr. Phys.*, *69*, 2355–2366, doi:10.1016/j.jastp.2007.06.010.
Iimura, H., S. E. Palo, Q. Wu, T. L. Killeen, S. C. Solomon, and W. R. Skinner (2009), Structure of the nonmigrating semidiurnal tide above Antarctica observed from the TIMED Doppler Interferometer, *J. Geophys. Res.*, *114*, D11102, doi:10.1029/2008JD010608.
Iimura, H., D. C. Fritts, Q. Wu, W. R. Skinner, and S. E. Palo (2010), Nonmigrating semidiurnal tide over the Arctic determined from TIMED Doppler Interferometer wind observations, *J. Geophys. Res.*, *115*, D06109, doi:10.1029/2009JD012733.
Kishore, P., S. P. Namboothiri, K. Igarashi, Y. Murayama, and B. J. Watkins (2002), MF radar observations of mean winds and tides over Poker Flat, Alaska (65.1°N, 147.5°W), *Ann. Geophys.*, *20*, 679–690.
Lau, E. M., S. K. Avery, J. P. Avery, S. E. Palo, and N. A. Makarov (2006), Tidal analysis of meridional winds at the South Pole using a VHF interferometric meteor radar, *J. Geophys. Res.*, *111*, D16108, doi:10.1029/2005JD006734.
Liu, H.-L., W. Wang, A. D. Richmond, and R. G. Roble (2010), Ionospheric variability due to planetary waves and tides for solar minimum conditions, *J. Geophys. Res.*, *115*, A00G01, doi:10.1029/2009JA015188.
Lübken, F.-J., J. Höffner, T. P. Viehl, B. Kaifler, and R. J. Morris (2011), First measurements of thermal tides in the summer mesopause region at Antarctic latitudes, *Geophys. Res. Lett.*, *38*, L24806, doi:10.1029/2011GL050045.
Manson, A. H., C. Meek, M. Hagan, X. Zhang, and Y. Luo (2004), Global distributions of diurnal and semidiurnal tides: Observations from HRDI UARS of the MLT region and comparisons with GSWM-02 (migrating and nonmigrating components), *Ann. Geophys.*, *22*, 1529–1548.
Manson, A. H., et al. (2006), Winter warmings, tides and planetary waves: Comparisons between CMAM (with interactive chemistry) and MFR-MetO observations and data, *Ann. Geophys.*, *24*, 2493–2518. [Available at http://www.ann-geophys.net/24/2493/2006/.]
Manson, A. H., et al. (2009), Arctic tidal characteristics at Eureka (80°N, 86°W) and Svalbard (78°N, 16°E) for 2006/07: Seasonal and longitudinal variations, migrating and non-migrating tides, *Ann. Geophys.*, *27*, 1153–1173. [Available at http://www.ann-geophys.net/27/1153/2009/.]
Mayr, H. G., J. G. Mengel, E. R. Talaat, H. S. Porter, and K. L. Chan (2005), Mesospheric non- migrating tides generated with planetary waves: I. Characteristics, *J. Atmos. Sol. Terr. Phys.*, *67*, 959–980.
McLandress, C. (1998), On the importance of gravity waves in the middle atmosphere and their parameterization in general circulation models, *J. Atmos. Sol. Terr. Phys.*, *60*, 1357–1383, doi:10.1016/S1364-6826(98)00061-3.
McLandress, C. (2002), The seasonal variation of the propagating diurnal tide in the mesosphere and lower thermosphere: Part 1. The role of gravity waves and planetary waves, *J. Atmos. Sci.*, *59*(5), 893–906, doi:10.1175/1520-0469(2002)059<0893:TSVOTP>2.0.CO;2.
McLandress, C., G. G. Shepherd, and B. H. Solheim (1996), Satellite observations of thermospheric tides: Results from the Wind Imaging Interferometer on UARS, *J. Geophys. Res.*, *101*, 4093–4114, doi:10.1029/95JD03359.
Merzlyakov, E. G., Y. I. Portnyagin, N. A. Makarov, J. Forbes, and S. Palo (2005), Eastward-propagating day-to-day wind oscillations in the northern polar mesosphere/lower thermosphere, *Atmos. Oceanic Phys.*, *41*, 92–104.
Mitchell, N. J., D. Pancheva, H. R. Middleton, and M. E. Hagan (2002), Mean winds and tides in the Arctic mesosphere and lower thermosphere, *J. Geophys. Res.*, *107*(A1), 1004, doi:10.1029/2001JA900127.
Miyahara, S., Y. Miyoshi, and K. Yamashita (1999), Variations of migrating and nonmigrating tides simulated by the middle atmosphere circulation model at Kyushu University, *Adv. Space Res.*, *24*, 1549–1558.
Murphy, D. J., et al. (2006), A climatology of tides in the Antarctic mesosphere and lower thermosphere, *J. Geophys. Res.*, *111*, D23104, doi:10.1029/2005JD006803.
Murphy, D. J., T. Aso, D. C. Fritts, R. E. Hibbins, A. J. McDonald, D. M. Riggin, M. Tsutsumi, and R. A. Vincent (2009), Source regions for Antarctic MLT non-migrating semidiurnal tides, *Geophys. Res. Lett.*, *36*, L09805, doi:10.1029/2008GL037064.
Norton, W. A., and J. Thuburn (1999), Sensitivity of mesospheric mean flow, planetary waves, and tides to strength of gravity wave drag, *J. Geophys. Res.*, *104*, 30,897–30,911, doi:10.1029/1999JD900961.
Nozawa, S., et al. (2005), Mean winds, tides, and quasi-2 day wave in the polar lower thermosphere observed in European Incoherent Scatter (EIS-CAT) 8 day run data in November 2003, *J. Geophys. Res.*, *110*, A12309, doi:10.1029/2005JA011128.
Ortland, D. A. (2005), Generalized Hough modes: The structure of damped global-scale waves propagating on a mean flow with horizontal and vertical shear, *J. Atmos. Sci.*, *62*, 2674–2683.
Oznovich, I., R. L. Walterscheid, G. G. Sivjee, and D. J. McEwen (1997), On Krassovsky's ratio for terdiurnal hydroxyl oscillations in the winter polar mesopause, *Planet. Space Sci.*, *45*(3), 385–394, doi:10.1016/S0032-0633(96)00130-4.
Palo, S. E., R. G. Roble, and M. E. Hagan (1998), TIME-GCM results for the quasi-two day wave, *Geophys. Res. Lett.*, *25*, 3783–3786, doi:10.1029/1998GL900032.
Portnyagin, Y. I., J. M. Forbes, and N. A. Makarov (1997), Unusual characteristics of lower thermosphere prevailing winds at South Pole, *Geophys. Res. Lett.*, *24*, 81–84.
Portnyagin, Y. I., J. M. Forbes, N. A. Makarov, E. G. Merzlyakov, and S. Palo (1998), The summertime 12-h wind oscillation with zonal wavenumber $s = 1$ in the lower thermosphere over the South Pole, *Ann. Geophys.*, *16*, 828–837.
Portnyagin, Y. I., et al. (2004), Monthly mean climatology of the prevailing winds and tides in the Arctic mesosphere/lower thermosphere, *Ann. Geophys.*, *22*, 3395–3410.
Scinocca, J. F., and N. A. McFarlane (2004), The variability of the modeled tropical precipitation, *J. Atmos. Sci.*, *61*(16), 1993–2015, doi:10.1175/1520-0469(2004)061<1993:TVOMTP>2.0.CO;2.
Singer, W., R. Latteck, P. Hoffman, B. P. Williams, D. C. Fritts, Y. Murayama, and K. Sakanoi (2005), Tides near the Arctic summer mesopause during the MaCWAVE/MIDAS summer program, *Geophys. Res. Lett.*, *32*, L07S90, doi:10.1029/2004GL021607.
Smith, A. K., and D. A. Ortland (2001), Modeling and analysis of the structure and generation of the terdiurnal tide, *J. Atmos. Sci.*, *58*(21), 3116–3134, doi:10.1175/1520-0469(2001)058<3116:MAAOTS>2.0.
Smith, A. K., D. V. Pancheva, N. J. Mitchell, D. R. Marsh, J. M. IIIRussell, and M. G. Mlynczak (2007), A link between variability of the semidiurnal tide and planetary waves in the opposite hemisphere, *Geophys. Res. Lett.*, *34*, L07809, doi:10.1029/2006GL028929.

Teitelbaum, H., and F. Vial (1991), On tidal variability induced by nonlinear interaction with planetary waves, *J. Geophys. Res.*, *96*, 14,169–14,178, doi:10.1029/91JA01019.

Ward, W. E., V. I. Fomichev, and S. Beagley (2005), Nonmigrating tides in equinox temperature fields from the Extended Canadian Middle Atmosphere Model (CMAM), *Geophys. Res. Lett.*, *32*, L03803, doi:10.1029/2004GL021466.

Ward, W. E., et al. (2010), On the consistency of model, ground-based and satellite observations of tidal signatures: Initial results from the CAWSES tidal campaigns, *J. Geophys. Res.*, *115*, D07107, doi:10.1029/2009JD012593.

Wu, Q., T. L. Killeen, S. Nozawa, D. McEwen, W. Guo, and S. C. Solomon (2003), Observations of mesospheric neutral wind 12 hour wave in the Northern Polar Cap, *J. Atmos. Terr. Phys.*, *65*, 971–978.

Xu, X., et al. (2009), Relationship between variability of the semidiurnal tide in the Northern Hemisphere mesosphere and quasi-stationary planetary waves throughout the global middle atmosphere, *Ann. Geophys.*, *27*, 4239–4256, doi:10.5194/angeo-27-4239-2009.

Yamashita, K., S. Miyahara, Y. Miyoshi, K. Kawano, and J. Ninomiya (2002), Seasonal variation of non-migrating semidiurnal tide in the polar MLT region in a general circulation model, *J. Atmos. Sol. Terr. Phys.*, *64*, 1083–1094.

Younger, P. T., D. Pancheva, H. R. Middleton, and N. J. Mitchell (2002), The 8-h tide in the Arctic mesosphere and lower thermosphere, *J. Geophys. Res.*, *107*(A12), 1420, doi:10.1029/2001JA005086.

Zhang, X., J. M. Forbes, M. E. Hagan, J. M. Russell, S. E. Palo, C. J. Mertens, and M. G. Mlynczak (2006), Monthly tidal temperatures 20–120 km from TIMED/SABER, *J. Geophys. Res.*, *111*, A10S08, doi:10.1029/2005JA011504.

Zeng, Z., W. Randel, S. Sokolovskiy, C. Deser, Y. H. Kuo, M. Hagan, J. Du, and W. E. Ward (2008), Detection of migrating diurnal tide in the tropical UTLS using the CHAMP radio occultation data, *J. Geophys. Res.*, *113*, D03102, doi:10.1029/2007JD008725.